

# Breathable and Skin-Conformal Electronics with Hybrid Integration of Microfabricated Multifunctional Sensors and Kirigami-Structured Nanofibrous Substrates

Hegeng Li, Zuo Chen Wang, Mingze Sun, Hengjia Zhu, Hongzhen Liu, Chuyang Y. Tang, and Lizhi Xu\*

Skin-integrated soft electronics have attracted extensive research attention due to their potential utility for fitness monitoring, disease management, human–machine interfaces, and other applications. Although many materials and device components are explored for the construction of skin-integrated systems, achieving multifunctional sensor platform combined with good breathability and conformability on the skin remains difficult. This challenge is partly due to the processing incompatibility between planar-fabricated microelectronics and biocompatible porous substrates. Here, a fabrication strategy that can overcome this limitation, leading to large-area multifunctional skin electronics with breathability and conformability required for wearable applications, is reported. In this scheme, a hybrid integration of high-performance microfabricated sensors and nanofibrous soft substrates is made possible with stamp-based transferring techniques combined with electrospinning. The resulting membrane devices exhibit tissue-like mechanical properties with high permeability for vapor transport. In addition, kirigami structures can be introduced into these membranes, providing high stretchability and 3D conformability for large-area integration on the skin. The multifunctional sensors array allow for spatiotemporal measurement of bioelectrical signals, temperature, skin hydration, and potentially many other physiological parameters. The robust performance and manufacturing scalability provided by these multifunctional skin electronics may create further opportunities for the development of advanced wearable systems.

## 1. Introduction

Skin-mounted electronic systems show great promise for the application in healthcare and human–machine interfaces.<sup>[1–6]</sup> These systems aim to monitor physiological parameters from the skin, which is the largest organ in the human body presenting abundant biophysical and biochemical signals. Ideal skin-electronics interfaces would require several essential features: 1) structural flexibility and conformability that accommodate large area of the skin contour; 2) arrays of high-performance sensors that enables spatiotemporal measurement in a reliable manner; and 3) biocompatibility and breathability of the devices that allow extended use in a wearable configuration.

Despite extensive effort over the past decade, achieving a combination of these essential attributes remains challenging. Biosensors built with traditional planar microfabrication techniques exhibit excellent electronic performances for physiological measurement,<sup>[7,8]</sup> but they usually involve planar and rigid substrates, which are not suited for large-area integration on the skin. Recent methods allowed for transfer printing of planar-fabricated electronics onto soft substrates.<sup>[9–11]</sup> However,


such devices are based on dense polymer films that hinders the transport of liquid and vapor. Their limited breathability represents a major concern for long-term application on the skin.

Alternatively, a variety of porous substrates involving woven fabrics,<sup>[12–14]</sup> electrospun membranes,<sup>[15,16]</sup> synthetic foams,<sup>[17,18]</sup> plant-derived materials,<sup>[19,20]</sup> etc., were exploited for the construction of wearable electronics with enhanced breathability. However, their integration with high-performance electronic sensors becomes difficult due to the incompatibility of processing conditions. In fact, electronic devices on porous substrates were usually constructed with infiltrated conductive inks based on carbon nanotubes,<sup>[21,22]</sup> metallic nanowires,<sup>[23,24]</sup> liquid metals,<sup>[25,26]</sup> conducting polymers,<sup>[27,28]</sup> or other components.<sup>[29,30]</sup> The required printing processes create difficulties for the patterning of high-density sensors array. The low

H. Li, Z. Wang, M. Sun, H. Zhu, H. Liu, L. Xu  
Department of Mechanical Engineering  
The University of Hong Kong  
Hong Kong SAR 999077, China  
E-mail: xulizhi@hku.hk

Z. Wang, L. Xu  
Advanced Biomedical Instrumentation Centre Limited  
Hong Kong SAR 999077, China

C. Y. Tang  
Department of Civil Engineering  
The University of Hong Kong  
Hong Kong SAR 999077, China

 The ORCID identification number(s) for the author(s) of this article can be found under <https://doi.org/10.1002/adfm.202202792>.

DOI: 10.1002/adfm.202202792

electrical conductivity from these inks also creates constraints for the sensory performance. Furthermore, design of multifunctional system becomes challenging due to the limited materials options that can be directly processed on porous substrates. Selective encapsulation of the electronics without compromising the structural permeability represents another concern.

Here, we report an approach to the manufacturing of breathable and skin-conformal electronics that can overcome the limitations described above. Specifically, a hybrid integration of high-performance sensors and breathable nanofibrous substrates was made possible with stamp-based transferring techniques followed by electrospinning. This manufacturing approach mitigates the processing incompatibility between planar microelectronic devices and porous substrates, leading to systems with excellent sensory performance in combination with breathability for long-term wearing on the skin. Furthermore, kirigami-inspired structures can be introduced in these membrane devices, allowing for large-area integration on the skin with conformal contact. The multifunctional sensors array enables continuous measurement of body temperature, electrocardiogram (ECG), skin hydration, electromyogram (EMG), and potentially other physiological parameters. The robust performance and manufacturing scalability provided by these electronics-skin interfaces may create advanced routes for wearable health monitoring, human–robot interaction, virtual/augmented reality, and many other applications.

## 2. Results and Discussion

Construction of the breathable and conformal electronic membranes (BCEMs) starts with fabrication of electronic components with stretchable serpentine patterns on a planar wafer (Figure 1a and Figure S1, Supporting Information). This process benefits from established techniques involving thin-film deposition, photolithography, etching, etc., which can generate a variety of high-performance electronics based on metals, semiconductors, and polymers. The active device components are selectively encapsulated with a polyimide (PI) layer ( $\approx 5 \mu\text{m}$  in thickness) to prevent crosstalk between sensors or current leakage. A sacrificial layer based on poly(methyl methacrylate) (PMMA) is placed between the electronic components and the planar substrate, allowing for release of the serpentine devices from the handling wafer after dissolving PMMA in acetone. Subsequently, the electronics can be picked up with a stamp (i.e., water-soluble tape) since the interaction between the device and the wafer is sufficiently weak after the dissolution of the sacrificial layer (Figure S2, Supporting Information). In the next step, polymer nanofibers (e.g., those from styrene-ethylene-butylene-styrene, or SEBS) are electrospun on top of stamp-supported devices, which serves as a porous substrate with desired flexibility and mass permeability. Other polymers (e.g., polyurethane or poly (lactic-co-glycolic acid)) that are suitable for electrospinning are also potential candidates for the construction of BCEMs. Indeed, this process is highly scalable since multiple device-on-stamps can be combined into a continuous membrane with roll-to-roll processing for electrospinning. In addition, variation of substrate materials and tuning of their

structural parameters can be achieved during the electrospinning process. Dissolving the water-soluble tapes yields free-standing membrane devices, which can be further processed with laser cutting to incorporate kirigami structures. Here, the periodic and alternating cuts endow high stretchability of the structures as well as their conformability on 3D curved surfaces (Figures S3 and S4, Supporting Information).<sup>[31,32]</sup> Round edges in the kirigami cuts are designed and implemented during the laser cutting process to mitigate stress concentration during deformation (Figure S3, Supporting Information).

Figure 1b shows a representative BCEM conformally laminated on the back of a healthy volunteer, covering  $\approx 300 \text{ cm}^2$  of the skin surface, and enlarged image (Figure 1c, left) shows serpentine electronics integrated on the BCEM. The tissue-like nanofibrous substrate affords conformal contact and adequate adhesion based on van der Waals interactions.<sup>[33]</sup> The dimension of the sensors array exceeded the size limit of individual handling wafer (4 inches in diameter), demonstrating the scalability of the integration process. The intrinsic flexibility of the SEBS nanofibers couples with the enhanced deformability arising from kirigami structures, which provide mechanical support for the intimate contact between sensors and the contoured skin surface (Figure 1c, right). In addition, the permeable nanofiber network (Figure 1d) ensures good breathability of membrane device. On the other hand, the serpentine configuration of the electronic components minimizes the mechanical restriction imposed to the membrane structures. As a proof of concept, we incorporated microfabricated bipolar electrodes, unipolar electrodes, temperature sensors, and hydration sensors into the device platform (Figure 1e). Indeed, many other devices involving inorganic semiconductors or biochemical reagent can be included during the fabrication process for extended functions.

We systematically characterized the behaviors of the BCEMs under mechanical deformation to evaluate their robustness during use. The physical integrity of the devices is ensured by sufficient adhesion between SEBS and PI layers, with an interfacial toughness of  $\approx 50 \text{ J m}^{-2}$  (Figure 2a). Furthermore, the kirigami patterns introduced in the membrane can accommodate large deformation without causing excessive stress which may cause interfacial delamination. Figure 2b illustrates the strain–stress curve of a BCEM (also in Figure S5a, Supporting Information). The device possesses ultra-low modulus of 5 kPa below 50% of tensile strain due to the stretchability of kirigami structures, which matches the regime of natural motion of human skin.<sup>[33,34]</sup> Under high elongation, the mechanical behavior of BCEMs is associated with the intrinsic deformation of the nanofibrous network, which is consistent with the responses of nanofibrous SEBS membranes without kirigami patterning (Figure S6, Supporting Information). The combination of kirigami structures and the serpentine electronic components confers deformation-invariant electrical performance (Figure 2c–e). As a BCEM was stretched uniaxially from 0% to 120%, there was negligible change in resistance ( $\Delta R/R_0$ ) for the serpentine interconnects even with severe distortion (Figure S7, Supporting Information). On the other hand, serpentine interconnects bonded to a continuous membrane without kirigami cuts experienced failure at a much lower tensile strain of 70%. The deformation-invariant electrical properties were also

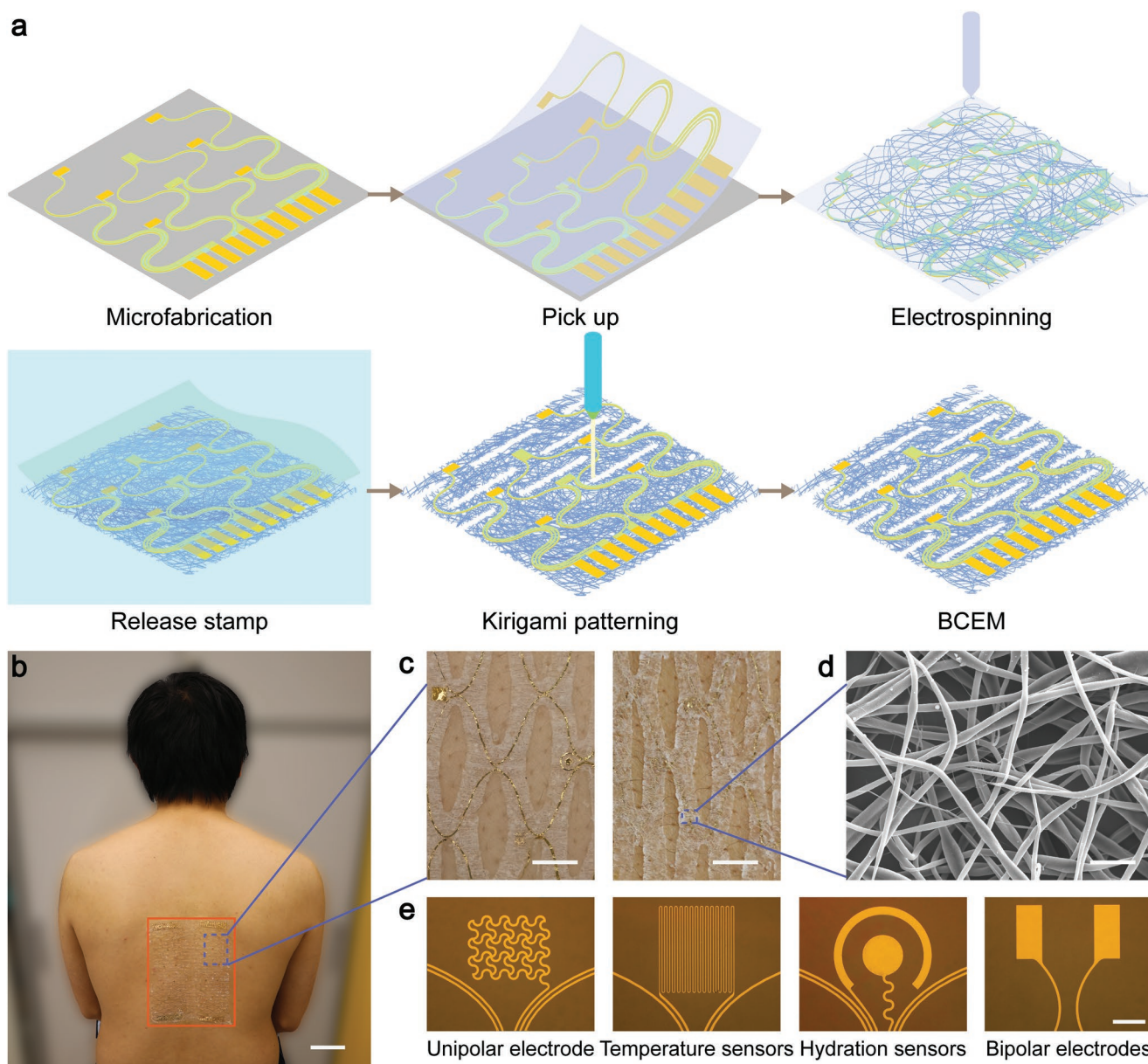


**Figure 1.** Breathable and conformal electronic membranes (BCEMs). a) Schematics of the fabrication process illustrating stamp-based transferring techniques, electrospinning, and kirigami patterning. b) A BCEM laminated on the back of a volunteer showing large-area skin integration. Scale bar: 5 cm. c) Photographs showing serpentine electronics on top of the nanofibrous substrate (left) and in conformal contact (right) with the skin surface. Scale bar: 10 mm. d) A scanning electron microscopy (SEM) image showing the permeable nanofibrous structure of a BCEM. Scale bar: 5  $\mu\text{m}$ . e) Optical microscope images of various microsensors built in a BCEM. Scale bar: 2 mm.

observed when the device was twisted by  $720^\circ$  (Figure 2d) or loaded with 10 000 cycles of 80% elongation (Figure 2e).

Finite element analysis (FEA) on BCEMs confirmed the strain tolerance of the devices. Under 25% of elongation, the deformation of kirigami structures accommodate the macroscopic stretching, and lead to only  $\approx 30$  kPa of stress in the serpentine interconnect (Figure 2g), which is well below the failure threshold for the constituent materials. In contrast, the membrane without kirigami would lead to stresses that are  $\approx 2$  times higher than those in the kirigami-structured membrane. Further details of FEA including mesh generation and stress

distribution of substrates are demonstrated in Figures S8 and S9 (Supporting Information). Indeed, the reduced stress levels associated with kirigami patterning are helpful for the prevention mechanical failure of electrical circuits and interfacial delamination. Furthermore, the deformability of BCEMs can be tuned with a variation of the cutting pattern, although the change of serpentine patterns may also require attention. The ultimate stretchability scales with  $\frac{L_c - x}{2\gamma}$ , where  $L_c$  is the length of the cut,  $x$  is the spacing between nearest cuts in the transverse direction, and  $\gamma$  is the spacing in the axial direction.<sup>[31]</sup> In



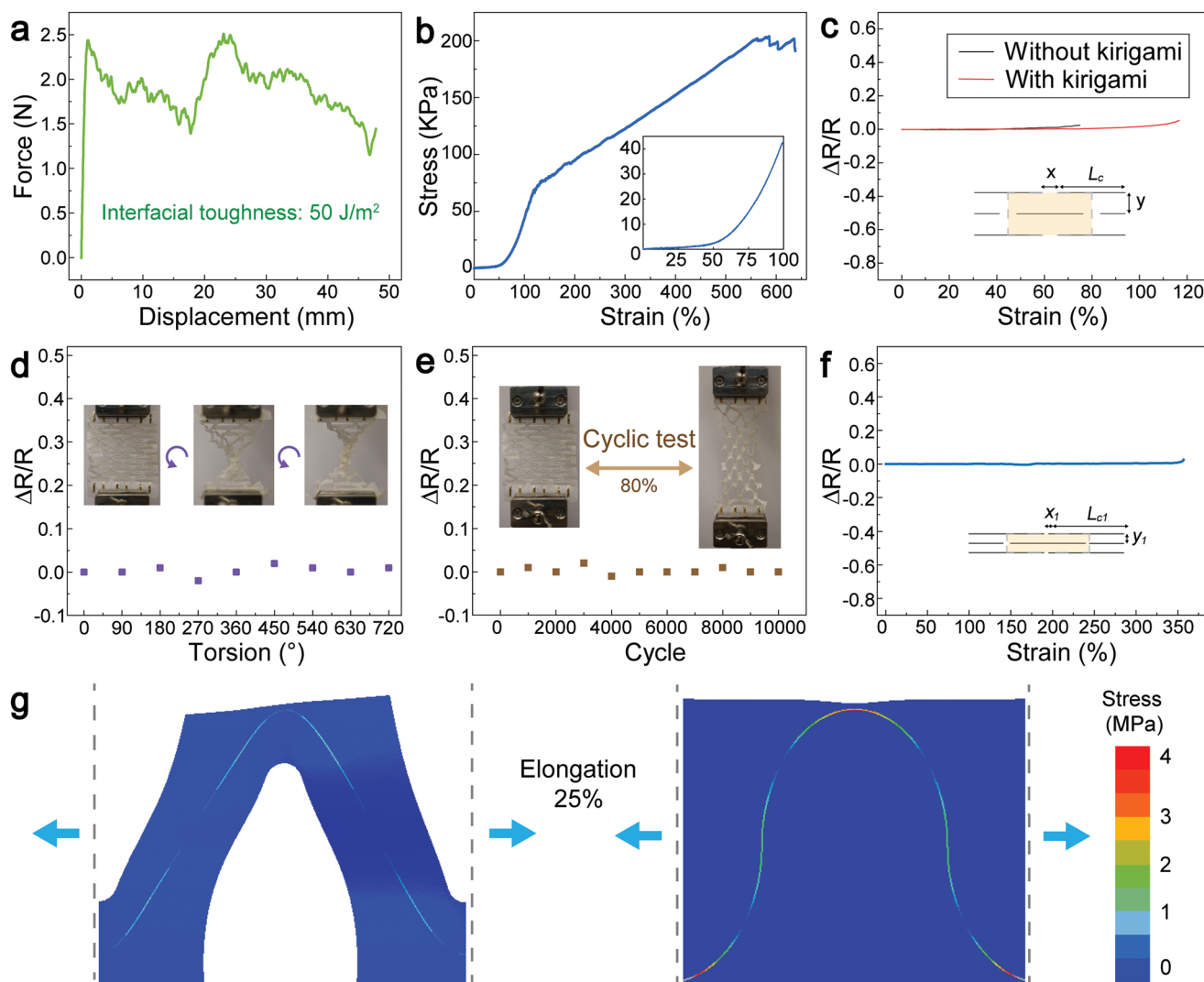


**Figure 2.** Mechanical behaviors of BCEMs. a) Characterization of interfacial toughness between microfabricated components (PI) and SEBS substrate. b) Stress-strain curve of a BCEM under tension. c) Resistance change of interconnects in a BCEM as a function of tensile strain, as compared with a similar membrane without kirigami patterning. d,e) Resistance change of interconnects in a BCEM with torsion up to 720° (d), or 10 000 cycles of 80% elongation (e). f) A variation of kirigami design leading to higher stretchability for the electrical interconnect. g) Finite element analysis (FEA) on the stress distribution in a BCEM under 25% of elongation, as compared with a device without kirigami cuts.

an alternative design, the stretchability of the electronic components can increase from  $\approx 120\%$  to  $\approx 350\%$ , as  $\gamma$  is reduced from 5 to 2 mm and  $x$  is reduced from 4 to 2 mm (Figure 2f and Figure S5b, Supporting Information).

The BCEMs exhibit good breathability and biocompatibility for skin-integration. Water vapor transmission rate (WVTR) serves as a key indicator of the breathability of membranes, and it is determined by measuring the weight loss of water-filled containers sealed with various membranes of interest.<sup>[35]</sup> The testing procedures were based on ASTM E96. Indeed, WVTR of a continuous SEBS nanofibrous membrane without kirigami cuts (Figure 3a) is eight times higher than that of a 100- $\mu\text{m}$ -thick polydimethylsiloxane (PDMS) film, which represents a common substrate for other skin-integrated soft electronics. The WVTR associated with nanofibrous substrates is similar to that of an open container without a cover. In addition,

the small spacing between open channels ( $<1\ \mu\text{m}$ ) in the nanofibrous membranes is unlikely to cause blockage of natural sweat pores, which is advantageous over perforated dense substrates with a typical spacing between pores on the order of  $\approx 100\ \mu\text{m}$ . The high vapor permeability of the substrate involved in BCEMs is advantageous for skin application, since sweat evaporation is essential for user comfort and the prevention of inflammation caused by perspiration accumulation. We performed on-skin tests to further demonstrate the breathability of the nanofibrous substrate (Figure 3e). Three films involving dense PDMS, dense SEBS, and nanofibrous SEBS were separately attached to the forearm of a healthy volunteer during a 30 min running exercise. We used an infrared camera to measure the skin temperatures before and after the exercise. In contrast to the dense films, the nanofibrous membrane induced little variation of the skin temperature during the exercise, indicating

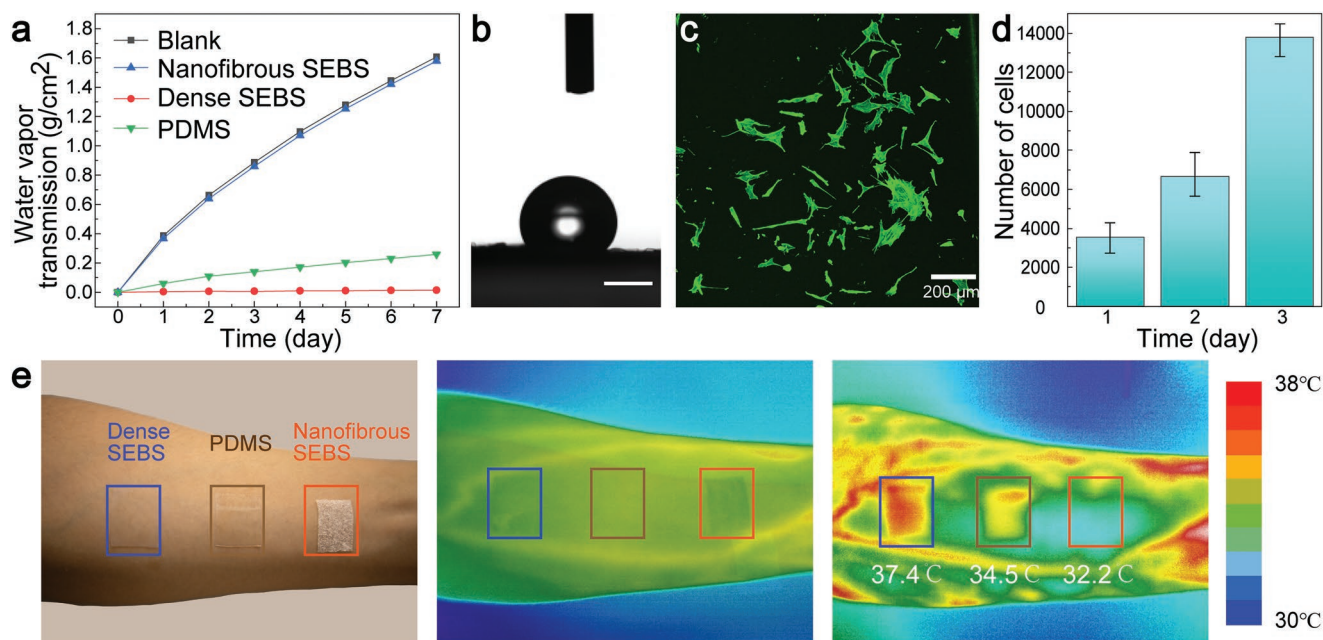


**Figure 3.** Breathability and biocompatibility of BCEMs. a) Water vapor transmission as a function of time for dense SEBS film, nanofibrous SEBS membrane, PDMS film, and blank control. b) A water droplet on a BCEM, showing the hydrophobicity provided by nanofibrous SEBS. Scale bar: 1 mm. c) A fluorescent image of fibroblasts cultured on a BCEM showing good cell viability and normal morphology. d) MTT assay showing cell proliferation on a BCEM over 3 days of incubation. e) A photograph (left) showing three different samples laminated on the forearm, and infrared thermal images before (middle) and after (right) the running exercise, demonstrating the breathability of a nanofibrous SEBS as compared with dense SEBS and PDMS film.

effective cooling by sweat evaporation. The hydrophobicity of SEBS was enhanced with the nanofibrous surface topography (Figure 3b and Figure S10, Supporting Information), which helps to prevent capillary forces that could damage the device. Biocompatibility of BCEMs were confirmed with cell culture experiments. Live/Dead assay on NIH 3T3 fibroblasts cultured on a representative device shows good viability and morphology of the cells (Figure 3c). In addition, cell proliferation over 3 days of incubation was quantified with MTT (3-[4,5-dimethylthiazol-2-yl]-2,5 diphenyl tetrazolium bromide) assay (Figure 3d).

A representative BCEM involves six unipolar electrodes, three temperature sensors, two hydration sensors, and one pair of bipolar electrodes for further integration with semiconductor optoelectronics (Figure S11, Supporting Information). Such array of sensors enables multi-modal physiological measurement on the skin. ECG signals were obtained from two BCEMs separately mounted on the left and right forearms of a healthy volunteer (Figure 4a). The contact impedance between the BCEM electrode and the skin is  $\approx 300$  k $\Omega$  at 100 Hz (Figure S12, Supporting Information), which is sufficient for gathering high-quality electrophysiological signals comparable to those obtained with commercial silver/silver chloride (Ag/AgCl) gel electrodes (Figure 4b). In addition, the ECG signals obtained with BCEMs were stable after doing exercise (Figure S13, Supporting Information) or over a continuous period of measurement (Figure S14, Supporting Information). The temperature sensors in BCEMs consist of serpentine traces of gold (Au, 20  $\mu$ m in width and 30nm in thickness), where changes in resistance correlate to the changes in temperature. The temperature coefficient of resistance for the sensors is  $4.3 \times 10^{-3} \text{ }^\circ\text{C}^{-1}$  in physiologically relevant range (Figure S15a, Supporting

Information). The functionality of temperature sensors was examined with cold compress applied on top of the skin where the sensor was laminated. The BCEM captured the temperature drop associated with the cold compress and the recovery to the baseline as the cold compress was removed. The temperature measured with BCEM is consistent with the results measured by a commercial thermocouple (Figure 4c). The hydration sensor involves coaxial dot-ring Au electrodes, which characterizes skin hydration through the measurement of electrical impedance. A commercial skin hydration sensor was used for the calibration for BCEMs in Figure S15b (Supporting Information). Figure 4d demonstrates the impedance captured by a BCEM as a function of skin hydration levels, measured at various frequencies. In another experiment, the natural attenuation of skin hydration levels after applying moisturizing lotion was measured with both commercial sensors and BCEM sensors. The hydration responses recorded by the two types of sensors are consistent, demonstrating the stable performance of the BCEM (Figure 4e).

EMG signals generated from the contraction of muscles are essential for medical diagnosis, control of prosthesis, human-robot interactions, virtual/augmented reality, and other technologies. We exploited BCEMs for EMG-based gesture recognition to demonstrate their potential for further applications. The large-area and conformal contact between BCEMs and the skin surface, along with their good breathability, are advantageous for spatiotemporal recording of EMG. Continuous measurement with BCEM electrodes generated EMG recordings with high signal quality (Figure 5a). To differentiate various gestures, we chose three pairs of electrodes mounted across the forearm of a healthy volunteer and obtained simultaneous

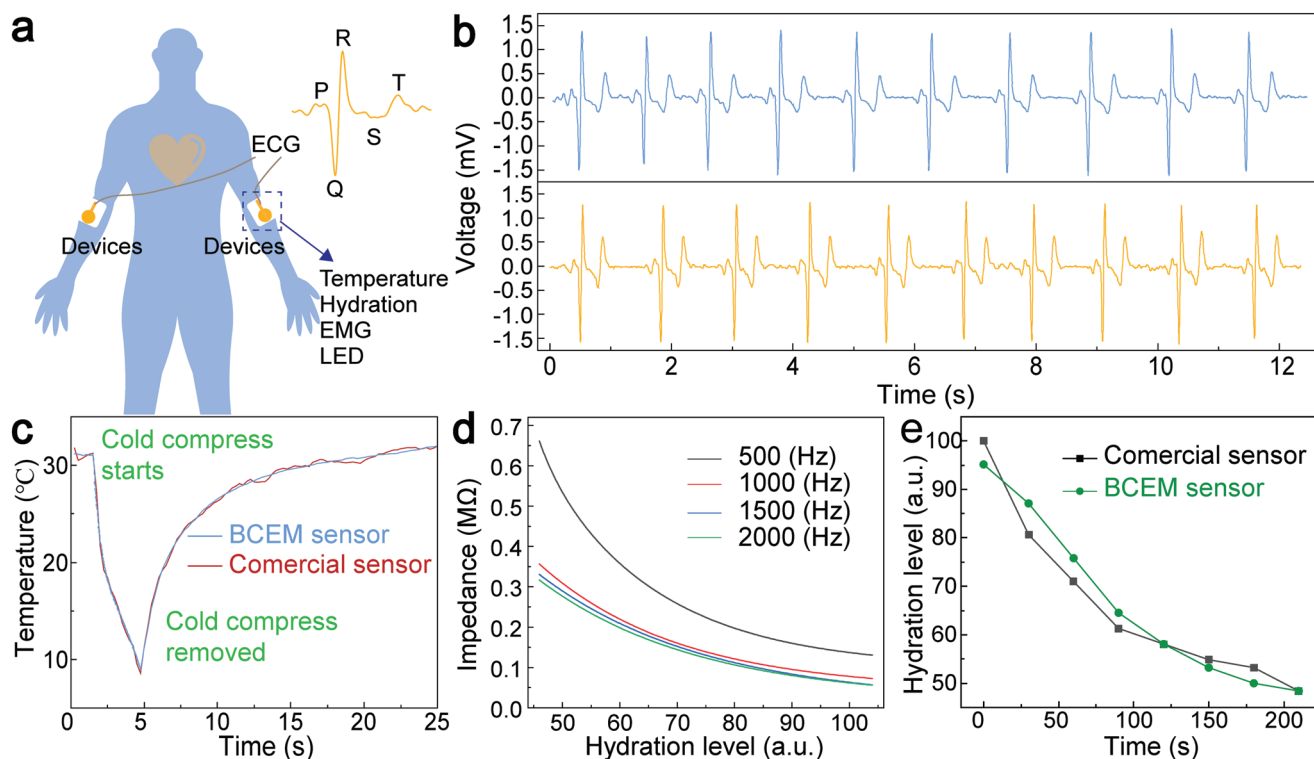


**Figure 4.** Multi-modal physiological sensing with BCEMs. a) A schematic showing the measurement scheme. b) Comparison of ECG signals detected by commercial gel electrodes (top) and BCEM (bottom). c) Temperature variation associated with cold compress applied on the skin, measured with a BCEM. d) Electrical impedance as a function of skin hydration, measured with coaxial electrodes on a BCEM under various frequencies. e) Decay of skin hydration after the application of moisturizing lotion, measured with both BCEM sensor and commercial sensor.

recordings from these three independent channels (Figure 5b). The five different modes of motion are distinguishable with the distinct activation patterns of EMG from the corresponding muscle groups (Figure 5c).

### 3. Conclusion

In summary, we have developed a route for hybrid integration of high-performance microsensors and nanofibrous substrates for the construction of breathable and skin-conformal electronics. The fabrication techniques mitigated the mismatches in processing conditions for various device components, allowing for scalable manufacturing of multifunctional devices tailored for skin-integration. The devices constructed with these techniques combine excellent sensory performance with breathability and conformability to the skin surfaces, which is advantageous for extended use as wearable systems. We have demonstrated their realistic applications involving spatiotemporal measurement of temperature, hydration, ECG, and EMG, and there could be many other functionalities built on this platform due to the versatility of planar microfabrication and transfer printing methods. Further consideration of semiconductor electronics, biochemical sensors, and micro-actuators for integration on these devices will expand their utility, creating advanced tools for disease management, human-machine interface, and other applications.

### 4. Experimental Section

**Device Fabrication:** Fabrication of BCEMs began with spin coating a thin layer of poly (methyl methacrylate) (PMMA) (Sigma-Aldrich, MW 350k) on a 4-inch silicon wafer, which serves as the sacrificial layer. An encapsulation layer of polyimide (PI) (Sigma-Aldrich, product #575 801) was spin-coated and cured on top of PMMA. Next, a bilayer of chromium (Cr, 5 nm) and gold (Au, 50 nm) was sputtered (Denton Desktop Pro) on the PI layer, followed by photolithography (AZ 5214 and URE-2000/35L) and wet etching to obtain the first metallic layer with a width of 20  $\mu\text{m}$ , serving as the temperature sensing element. The second metallic layer consisting of Cr (5 nm) and Au (200 nm) was deposited and patterned for electrodes, hydration sensors, and interconnects. Another PI encapsulation layer was applied on top of the sensor components, and the overall structures of the serpentine devices were defined with reactive ion etching (RIE, Tailong Electronics) with oxygen-plasma, which completed the microfabrication process.

Water-soluble tapes (3M) were used to pick up the planar fabricated microdevices after dissolving PMMA in acetone for 12h. SEBS powders (H1062; Asahi Kasei) were dissolved in chloroform/toluene (8:2) to form a 15 wt.% SEBS solution. The tape-supported microsensors were anchored on the rolling substrate of an electrospinning equipment (Beijing Yongkang Co. Ltd.) to manufacture SEBS nanofibrous membranes. After releasing the tape in water, laser cutting was employed to obtain the kirigami pattern in BCEMs.

**FEA Simulation:** Static analysis was employed to predict the stress distribution in a kirigami sheet bonded with serpentine interconnects using a commercial software package (ABAQUS). The Young's moduli ( $E$ ) and Poisson's ratio ( $\nu$ ) of the materials used in the simulations are  $E_{\text{interconnects}} = 100 \text{ MPa}$ , and  $\nu_{\text{interconnects}} = 0.4$  for interconnects, and  $E_{\text{substrate}} = 1 \text{ MPa}$  and  $\nu_{\text{substrate}} = 0.3$  for substrate. Shell elements were applied to the model to get fine mesh distribution which can achieve the convergence



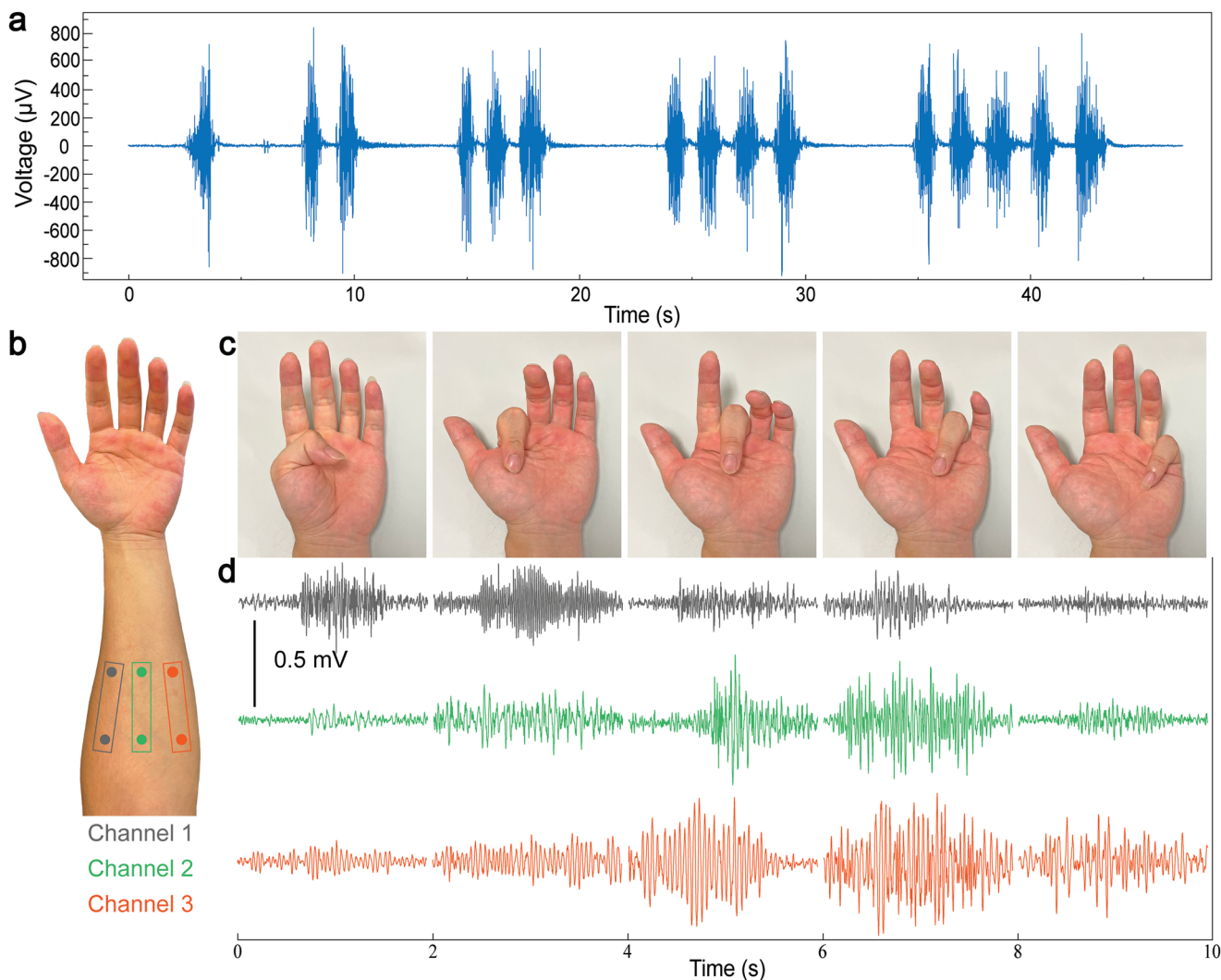


**Figure 5.** EMG recordings and gesture recognition with BCEMs. a) EMG signals arising from a pattern of hand motion. b) The locations of three pairs of EMG electrodes mounted on the forearm, forming three independent channels for data acquisition. c,d) Photographs of five different gestures (c), and the distinct patterns recorded by the three EMG channels (d).

of the nonlinear problem. A small perturbation was added in the Z-axis direction, so that the kirigami film can achieve 3D out-of-plane deformation.

**Cell Culture and Biocompatibility:** NIH 3T3 fibroblasts were used to examine the in vitro cytotoxicity of BCEMs. After disinfecting using ethyl alcohol, BCEMs were irradiated with UVO to improve surface energy to facilitate the adhesion of fibronectin. BCEMs were soaked in fibronectin for 24 h and then seeded with the cell suspension. After 24 h of incubation, the cells were observed using confocal fluorescent microscope (Nikon, Japan). MTT assay was used to quantify the cell proliferation. The absorption at 540 nm, which reflects the cell metabolic activity, was detected using a plate reader (BioTek, US). All samples were cultured at 37 °C in an incubator with 5% CO<sub>2</sub>.

**Characterization and Equipment:** Scanning electron microscopy (SEM) images of BCEM were taken with Hitachi S4800. Mechanical characterization and interfacial toughness were carried out with Zwick Roell tensile tester. A digital source meter (2450; Keithley Instruments) was applied to record the variation of resistance upon uniaxial tensile and cyclic testing. The interfacial toughness was determined by dividing the plateau force by the width of the SEBS sheet.<sup>[36]</sup> Hydrophobicity of the membranes was measured with a video water contact angle system (VCA 2500XE; AST Products). Electrophysiological signals were measured using a commercial data acquisition system (PowerLab T26, AD Instruments). Adding a layer of conductive gel (SignaGel Electrode Gel, USA) between

electrodes and the skin improved the signal quality for electrophysiological measurements. Impedance/resistance for skin hydration and temperature were recorded with a LCR meter (E4980AL; Keysight Instruments). The calibration for the skin hydration sensor was done with a commercial hydrometer (Real Bubee). Thermal images were taken with an infrared imaging camera (Fluke Ti480). All human experiments were performed upon approval from the Human Research Ethics Committee, The University of Hong Kong under grant number EA1812001. In addition written consent was acquired from the participants of the research.

## Supporting Information

Supporting Information is available from the Wiley Online Library or from the author.

## Acknowledgements

The study was supported by Research Grants Council (RGC), University Grants Committee (UGC) (Project 27210019 and 17200320). The authors thank Dr. W. X. and Dr. B. Y. for fruitful discussion and assistance on experiments.

## Conflict of Interest

The authors declare no conflict of interest.

## Data Availability Statement

The data that support the findings of this study are available from the corresponding author upon reasonable request.

## Keywords

breathability, kirigami devices, nanofibers, physiological monitoring, skin-integrated electronics

Received: March 10, 2022

Revised: May 5, 2022

Published online:

- [1] C. Wang, C. Wang, Z. Huang, S. Xu, *Adv. Mater.* **2018**, *30*, 1801368.
- [2] H. Li, H. Liu, M. Sun, Y. Huang, L. Xu, *Adv. Mater.* **2020**, *33*, 2004425.
- [3] Y. Zhang, T. Zhang, Z. Huang, J. Yang, *Adv. Sci.* **2022**, 2105084.
- [4] D. Jung, C. Lim, H. J. Shim, Y. Kim, C. Park, J. Jung, S. I. Han, S. Sunwoo, K. W. Cho, G. D. Cha, D. C. Kim, J. H. Koo, J. H. Kim, T. Hyeon, D. Kim, *Science* **2021**, *373*, 1022.
- [5] S. Guo, K. Wu, S. Guo, K. Wu, C. Li, H. Wang, Z. Sun, D. Xi, S. Zhang, *Matter* **2021**, *4*, 969.
- [6] Z. Zhu, S.-Z. Guo, T. Hirdler, C. Eide, X. Fan, J. Tolar, M. C. McAlpine, *Adv. Mater.* **2018**, *30*, 1707495.
- [7] S. Hong, N. Zagni, S. Choo, N. Liu, S. Baek, A. Bala, H. Yoo, B. H. Kang, H. J. Kim, H. J. Yun, M. A. Alam, S. Kim, *Nat. Commun.* **2021**, *12*, 3559.
- [8] J. J. Jun, N. A. Steinmetz, J. H. Siegle, D. J. Denman, M. Bauza, B. Barbarits, A. K. Lee, C. A. Anastassiou, A. Andrei, Ç. Aydin, M. Barbic, T. J. Blanche, V. Bonin, J. Couto, B. Dutta, S. L. Gratiy, D. A. Gutnisky, M. Häusser, B. Karsh, P. Ledochowitsch, C. M. Lopez, C. Mitelut, S. Musa, M. Okun, M. Pachitariu, J. Putzeys, P. D. Rich, C. Rossant, W. L. Sun, K. Svoboda, et al, *Nature* **2017**, *551*, 232.
- [9] Z. Huang, Y. Hao, Y. Li, H. Hu, C. Wang, A. Nomoto, T. Pan, Y. Gu, Y. Chen, T. Zhang, W. Li, Y. Lei, N. H. Kim, C. Wang, L. Zhang, J. W. Ward, A. Maralani, X. Li, M. F. Durstock, A. Pisano, Y. Lin, S. Xu, *Nat. Electron.* **2018**, *1*, 473.
- [10] H. Lee, C. Song, Y. S. Hong, M. S. Kim, H. R. Cho, T. Kang, K. Shin, S. H. Choi, T. Hyeon, D. Kim, *Sci. Adv.* **2017**, *3*, e1601314.
- [11] Z. Rao, Y. Lu, Z. Li, K. Sim, Z. Ma, J. Xiao, C. Yu, *Nat. Electron.* **2021**, *4*, 513.
- [12] L. Wang, X. Fu, J. He, X. Shi, T. Chen, P. Chen, B. Wang, H. Peng, *Adv. Mater.* **2020**, *32*, 1901971.
- [13] G. Chen, X. Xiao, X. Zhao, T. Tat, M. Bick, J. Chen, *Chem. Rev.* **2022**, *122*, 3259.
- [14] K. I. Jang, S. Y. Han, S. Xu, K. E. Mathewson, Y. Zhang, J. W. Jeong, G. T. Kim, R. C. Webb, J. W. Lee, T. J. Dawidczyk, R. H. Kim, Y. M. Song, W. H. Yeo, S. Kim, H. Cheng, S. Il Rhee, J. Chung, B. Kim, H. U. Chung, D. Lee, Y. Yang, M. Cho, J. G. Gaspar, R. Carbonari, M. Fabiani, G. Gratton, Y. Huang, J. A. Rogers, *Nat. Commun.* **2014**, *5*, 4779.
- [15] C. Tan, Z. Dong, Y. Li, H. Zhao, X. Huang, Z. Zhou, J.-W. Jiang, Y.-Z. Long, P. Jiang, T.-Y. Zhang, *Nat. Commun.* **2020**, *11*, 3530.
- [16] Z. Li, M. Zhu, J. Shen, Q. Qiu, J. Yu, B. Ding, *Adv. Funct. Mater.* **2019**, *30*, 1908411.
- [17] H. Guo, Y. J. Tan, G. Chen, Z. Wang, G. J. Susanto, H. H. See, Z. Yang, Z. W. Lim, L. Yang, B. C. K. Tee, *Nat. Commun.* **2020**, *11*, 5747.
- [18] C. W. Visser, D. N. Amato, J. Mueller, J. A. Lewis, *Adv. Mater.* **2019**, *31*, 1904668.
- [19] Q. Fu, Y. Chen, M. Sorieul, *ACS Nano* **2020**, *14*, 3528.
- [20] H. Zhu, W. Luo, P. N. Ciesielski, Z. Fang, J. Y. Zhu, G. Henriksson, M. E. Himmel, L. Hu, *Chem. Rev.* **2016**, *116*, 9305.
- [21] B. Zou, Y. Chen, Y. Liu, R. Xie, Q. Du, T. Zhang, Y. Shen, B. Zheng, S. Li, J. Wu, *Adv. Sci.* **2019**, *6*, 1801283.
- [22] L. Wang, L. Wang, Y. Zhang, J. Pan, S. Li, X. Sun, B. Zhang, H. Peng, *Adv. Funct. Mater.* **2018**, *28*, 1804456.
- [23] Y. J. Fan, X. Li, S. Y. Kuang, L. Zhang, Y. H. Chen, L. Liu, K. Zhang, S. W. Ma, F. Liang, T. Wu, *ACS Nano* **2018**, *12*, 9326.
- [24] Y. Xu, B. Sun, Y. Ling, Q. Fei, Z. Chen, X. Li, P. Guo, N. Jeon, S. Goswami, Y. Liao, S. Ding, Q. Yu, J. Lin, G. Huang, Z. Yan, *Proc. Natl. Acad. Sci. USA* **2020**, *117*, 205.
- [25] Z. Ma, Q. Huang, Q. Xu, Q. Zhuang, X. Zhao, Y. Yang, H. Qiu, Z. Yang, C. Wang, Y. Chai, Z. Zheng, *Nat. Mater.* **2021**, *20*, 859.
- [26] M. D. Dickey, *Adv. Mater.* **2017**, *29*, 1606425.
- [27] K. Qi, J. He, H. Wang, Y. Zhou, X. You, N. Nan, W. Shao, L. Wang, B. Ding, S. Cui, *ACS Appl. Mater. Interfaces* **2017**, *9*, 42951.
- [28] C. Lu, X. Chen, *Adv. Mater. Technol.* **2019**, *4*, 1900564.
- [29] N. Matsuhisa, D. Inoue, P. Zalar, H. Jin, Y. Matsuba, A. Itoh, T. Yokota, D. Hashizume, T. Someya, *Nat. Mater.* **2017**, *16*, 834.
- [30] Y. Wang, L. Yin, Y. Bai, S. Liu, L. Wang, Y. Zhou, C. Hou, Z. Yang, H. Wu, J. Ma, Y. Shen, P. Deng, S. Zhang, T. Duan, Z. Li, J. Ren, L. Xiao, Z. Yin, N. Lu, Y. A. Huang, *Sci. Adv.* **2020**, *6*, eabd0996.
- [31] T. C. Shyu, P. F. Damasceno, P. M. Dodd, A. Lamoureux, L. Xu, M. Shlian, M. Shtein, S. C. Glotzer, N. A. Kotov, *Nat. Mater.* **2015**, *14*, 785.
- [32] R. Zhao, S. Lin, H. Yuk, X. Zhao, *Soft Matter* **2018**, *14*, 2515.
- [33] D. H. Kim, N. Lu, R. Ma, Y. S. Kim, R. H. Kim, S. Wang, J. Wu, S. M. Won, H. Tao, A. Islam, K. J. Yu, T. Il Kim, R. Chowdhury, M. Ying, L. Xu, M. Li, H. J. Chung, H. Keum, M. McCormick, P. Liu, Y. W. Zhang, F. G. Omenetto, Y. Huang, T. Coleman, J. A. Rogers, *Science* **2011**, *333*, 838.
- [34] C. Dagdeviren, Y. Shi, P. Joe, R. Ghaffari, G. Balooch, K. Uskaonkar, O. Gur, P. L. Tran, J. R. Crosby, M. Meyer, Y. Su, R. C. Webb, A. S. Tedesco, M. J. Slepian, Y. Huang, J. A. Rogers, *Nat. Mater.* **2015**, *14*, 728.
- [35] B. Sun, R. N. McCay, S. Goswami, Y. Xu, C. Zhang, Y. Ling, J. Lin, Z. Yan, *Adv. Mater.* **2018**, *30*, 1804327.
- [36] H. Yuk, T. Zhang, S. Lin, G. A. Parada, X. Zhao, *Nat. Mater.* **2016**, *15*, 190.